

NCAR Global Model Topography Generation Software for Unstructured Grids

Peter H. Lauritzen¹, Julio T. Bacmeister¹, and Patrick F. Callaghan¹

¹National Center for Atmospheric Research, 1850 Table Mesa Drive, Boulder, Colorado, USA

Correspondence to: Peter Hjort Lauritzen
(pel@ucar.edu)

Abstract. TEXT

1 Introduction

define acronym CAM in introduction

Accurate representation of the impact of topography on atmospheric flow is crucial for Earth system modeling. For example, on the regional scale the hydrological cycle is closely linked to topography and, on the planetary scale, waves associated with the mid-latitude jets are very susceptible to the effective drag caused by mountains (e.g., Lott and Miller, 1997). Atmospheric blocking producing heat waves and droughts as well as atmospheric rivers are closely related to topographic forcing. Despite the fact that surface elevation is known globally to within a meter (or less), its representation in numerical models remains a challenge.

The interaction between topography and dynamics in numerical models is usually split into components:

- Resolved scale representation of topography in the dynamical core.
- Representation of sub-grid processes: e.g. unresolved gravity waves, low-level jet blocking, and turbulence forced by topography that result in a mean drag on the resolved-scale flow.

These two components are discussed in sub-sections below as well as the topographic input data typically needed by numerical models.

1.1 Resolved-scale topography: Surface geopotential Φ_s

The resolved scale component is basically the surface geopotential Φ_s , or, equivalently¹, the mean elevation in each grid box h . The ‘raw’ elevation data is usually from a digital elevation model (DEM) such as the GTOPO30; a 30 arc second global dataset from the United States Geological Survey (USGS; Gesch and Larson, 1998) defined on an approximately 1km regular latitude-longitude grid. Several newer, more accurate, and locally higher resolution elevation datasets are available such as GLOBE (GLOBE Task Team and others, 1999) and the NASA Shuttle Radar Topographic Mission (SRTM) DEM data (Farr et al., 2007). The SRTM data, however, is only near-global (up to 60° North and South).

For models based on a terrain-following coordinate the specification of Φ_s determines the location of vertical levels in that the levels closer to the surface has gradients proportional to the surface elevation. Hence the terrain-following coordinates are not perpendicular to the direction of the stratification (the radial direction) so errors can arise when calculations are needed along stratified layers. For example, the pressure-gradient force (PGF) in terrain-following coordinates splits into two terms; one that is proportional to the geopotential gradient and one that is proportional to the pressure gradient. These terms are of similar magnitude but opposite sign. For a perfectly balanced flow these terms should exactly cancel. Failure to preserve this balance can produce large spurious vertical velocities. This problem, referred to as the PGF error/problem, has significant implications for global atmospheric modeling, with efforts to tackle this problem stretching back as far as the late 1970s (Janjic, 1977; Mihailović and Janjić, 1986). As global models reach finer

¹if gravity is assumed constant

spatial scales, the pressure gradient problem leads to an increasingly polluted dynamical solution near steep topography since an increase in horizontal resolution, in general, steepen slopes.

When performing a spectral analysis of the raw elevation data, it is clear that Earth's topography decreases quite slowly with increasing wave number (see, e.g., Balmino, 1993). Consequently, there will always be a non-negligible spectral component of topography present near the grid scale at current and any foreseeable model resolution. It is common practice not to force the highest wave numbers directly in the model to alleviate obvious spurious noise (e.g. Navarra et al., 1994; Lander and Hoskins, 1997). Hence the raw topographic data is filtered to remove the highest wave numbers. There seem to be no standardized procedure, for example a test case suite, to objectively select level of smoothing and filtering method.

While it is necessary to smooth topography to remove spurious grid-scale noise, it introduces two problems. Filtering will typically raise ocean points near step topography to non-zero elevation. Perhaps the most striking example is the Andes mountain range that extends one or two grid cells into the Pacific after the filtering operation (Figure??). Ocean and land points are treated separately in weather/climate models so raised sea-points may potentially be problematic. Secondly, the filtering will generally reduce the height of local topographic maxima and given the importance of barrier heights in atmospheric dynamics, this could be a problem for the global angular momentum budget and could fundamentally change the flow.

To capture the barrier effect (blocking) that is sub-grid scale with respect to the smoothed topography, one may use *envelope topography* that adjusts the surface height with sub-grid scale topographic variance (Wallace et al., 1983). Loosely speaking, the peak heights are raised. A similar approach, but implemented as variational filtering, is taken in Rutt et al. (2006); this method also imposes additional constraints such as enforcing zero elevation over ocean masks.

As mentioned above it is not straight forward to determine how to smooth topography. One approach is to try different filtering methods in the full model and evaluate the results in weather forecasts or longer climate simulations (Navarra et al., 1994; Bouteloup, 1995, 1996). While this approach is certainly valuable, clearly the size of the Gibbs oscillations in global spectral models is reduced by smoothing topography, it does not take into account the interaction between the resolved-scale flow (dynamical core) and parameterizations of sub-grid scale processes (e.g., gravity wave drag, turbulent mountain stress). This interaction can be difficult to predict and commonly the sub-grid scale parameterization have been tuned over a number of years with the 'default' smoothed surface elevation. Hence, this methodology runs the risk of deeming one smoothing less accurate than another due to lack of optimum tuning (and/or complexity) of the parameterizations.

Another approach is to use idealized simulation with no parameterizations to determine what scales are adequately resolved and which are poorly resolved. Davies and Brown (2001) kept the physical scale of an idealized two-dimensional and three-dimensional isolated hill fixed and observed how the coarser resolution results differ from the high-resolution simulation. This can then provide guide-lines on how to smooth topography in the full model. Similar idealized (shallow water) experiments were used in Rutt et al. (2006) to optimally smooth topography. While these idealized tests provide a 'cleaner' approach to smoothing terrain, they do not consider the coupling with sub-grid scale processes in the sense that the high resolution solution may resolve gravity waves that the lower resolution simulation does not so in a sense the lower resolution model should include a parameterization for the gravity waves below a certain scale.

1.2 Sub-grid-scale topography:

On the sub-grid scale there are many processes associated with topography such as sub-grid blocking, flow splitting, sheltering effects, generation of turbulence by roughness and gravity wave breaking (Bougeault et al., 1990). Only a brief overview of common parameterizations is given here.

Turbulent drag may be parameterized either through 'effective roughness lengths' (Fiedler and Panofsky, 1972) or specified with an explicit topographic stress profile (introduced by Wood et al. (2001) and used by Beljaars et al. (2004)). These parameterizations are referred to as turbulent mountain stress (TMS); a form drag exerted by sub-grid scale topography (Richter et al., 2010). To better capture the blocking of low-level flow, blocking parameterizations may be used (ECMWF; Lott and Miller, 1997) and/or envelope topography. Similar schemes have since been widely adopted by other forecasting centers due to their clearly beneficial impacts on model performance (e.g. Webster et al., 2003b; Zadra et al., 2003; Kim and Doyle, 2005). Scinocca and McFarlane (2000) reported positive impact on global climate simulations from introducing a low-level blocking parameterization in the Canadian Center for Climate Modeling and Analysis GCM.

Vertically propagating gravity waves may break and slow down large scale flow. Parameterizations for that are referred to as gravity wave drag (GWD; Eckermann and Chun, 2003) [Julio: earlier reference?]. Many of these schemes also incorporate the effects of topographic anisotropy, i.e., the existence of ridges with dominant orientations, in determining the direction and magnitude of the drag exerted by sub-grid topography. The importance of anisotropy in quantifying topographic effects has been recognized for some time (e.g., Baines and Palmer, 1990; Bacmeister, 1993).

1.3 Topographic model input data

The data needed by the atmospheric model is, first of all, the surface geopotential on the models grid: Φ_s . The topographic input data for GWD and TMS are denoted *SGH* and *SGH30* (following CAM naming conventions), respectively. ¹⁶⁵ *SGH30* is the variance of Φ_s on horizontal scales smaller than approximate 3-5 km and *SGH* is the variance of topography on scales larger than 3-5km and up to the model grid scale. The separation scale is, loosely speaking, determined from linear theory that predict that gravity waves propagate ¹⁷⁰ in the vertical when the scale of a mountain is approximately larger than 3-5km (e.g., Durran, 2010; Beljaars et al., 2004). ¹⁷⁵ [we could consider showing some results - especially since CAM5.4/5 is using the new topo]].

Julio: please describe input data of ridges ...

In this paper we present a versatile software package for generating topographic model input data that directly supports unstructured grids. In addition to specifying Φ_s on the model ¹⁸⁰ grid a separation of sub-grid scales is needed for GWD and TMS. This separation of scales is done through an intermediate mapping of the raw elevation data to 3km cubed-sphere grid before mapping fields to the target model grid (Figure 1). This two-step process is described in section 2.2 after a mathematical definition of the separation involved in section 2.1. In section 2.2.3 the smoothing of Φ_s is discussed followed by ¹⁸⁵ a description of the algorithm for identifying sub-grid scale ridges (section 2.2.4).

190 2 Method

2.1 Continuous: separation of scales

The separation of scales is, in continuous space, conveniently introduced using spherical harmonics. Assume that elevation (above sea level) is a smooth continuous function in ¹⁹⁵ which case it can be represented by a convergent expansion of spherical harmonic functions of the form ²⁰⁰

$$h(\lambda, \theta) = \sum_{m=-\infty}^{\infty} \sum_{n=|m|}^{\infty} \psi_{m,n} Y_{m,n}(\lambda, \theta), \quad (1)$$

(e.g., Durran, 2010) where λ and θ are longitude and latitude, respectively, $\psi_{m,n}$ are the spherical harmonic coefficients. ²⁰⁵

Each spherical harmonic function is given in terms of the associated Legendre polynomial $P_{m,n}(\theta)$:

$$Y_{m,n} = P_{m,n}(\theta) e^{im\lambda} \quad (2)$$

where m is the zonal wavenumber and $m - |n|$ is the number of zeros between the poles and can therefore be interpreted as meridional wavenumber. ²⁴⁵

For the separation of scales of the variance of sub-grid-scale elevation the spherical harmonic expansion is truncated ²⁵⁰

at wavenumber M

$$h^{(M)}(\lambda, \theta) = \sum_{m=-M}^{\infty} \sum_{n=|m|}^M \psi_{m,n}^{(M)} Y_{m,n}(\lambda, \theta), \quad (3)$$

where a triangular truncation, which provides a uniform spatial resolution over the entire sphere, is used.

Let $h^{(tgt)}(\lambda, \theta)$ be a continuous representation of the elevation containing the spatial scales of the target grid. We do not write that in terms of spherical harmonics as the target grid may be variable resolution and therefore contains different spatial scales in different parts of the domain.

For each target grid cell Ω_k , $k = 1, \dots, N_t$, where N_t is the number of target grid cells, define the variances

$$\begin{aligned} \text{Var}_{\Omega_k}^{(tms)} &= \iint_{\Omega_k} [h^{(M)}(\lambda, \theta) - h(\lambda, \theta)]^2 \cos(\theta) d\lambda d\theta, \quad (4) \\ \text{Var}_{\Omega_k}^{(gwd)} &= \iint_{\Omega_k} [h^{(tgt)}(\lambda, \theta) - h^{(M)}(\lambda, \theta)]^2 \cos(\theta) d\lambda d\theta \end{aligned}$$

So $\text{Var}_{\Omega_k}^{(tms)}$ is the variance of elevation on scales below wavenumber M and $\text{Var}_{\Omega_k}^{(gwd)}$ is the variance of elevation on scales larger than wavenumber M and below the target grid scale. *SGH* and *Var*????

[julio: continuous definition of dominant orientation of topography with this notation?]

2.2 Discrete

The separation of scales is done through the use of a quasi-isotropic gnomonic cubed-grid grid in a two-step regridding procedure, that is, binning from source grid Λ to intermediate grid A (separation of scales) to target grid Ω .

Any quasi-uniform spherical grid could, in theory, be used for the separation of scales. For reasons that will become clear we have chosen to use a gnomonic cubed-sphere grid resulting from an equi-angular gnomonic (central) projection

$$x = r \tan \alpha \quad \text{and} \quad y = r \tan \beta; \quad \alpha, \beta \in \left[-\frac{\pi}{4}, \frac{\pi}{4}\right], \quad (6)$$

(Ronchi et al., 1996) where α and β are central angles in each coordinate direction, $r = R/\sqrt{3}$ and R is the radius of the Earth. A point on the sphere is identified with the three-element vector (x, y, ν) , where ν is the panel index. Hence the physical domain S (sphere) is represented by the gnomonic (central) projection of the cubed-sphere faces, $\Omega^{(\nu)} = [-1, 1]^2$, $\nu = 1, 2, \dots, 6$, and the non-overlapping panel domains $\Omega^{(\nu)}$ span the entire sphere: $S = \bigcup_{\nu=1}^6 \Omega^{(\nu)}$. The cube edges, however, are discontinuous. Note that any straight line on the gnomonic projection (x, y, ν) corresponds to a great-circle arc on the sphere. In the discretized scheme we let the number of cells along a coordinate axis be N_c so that the total number of cells in the

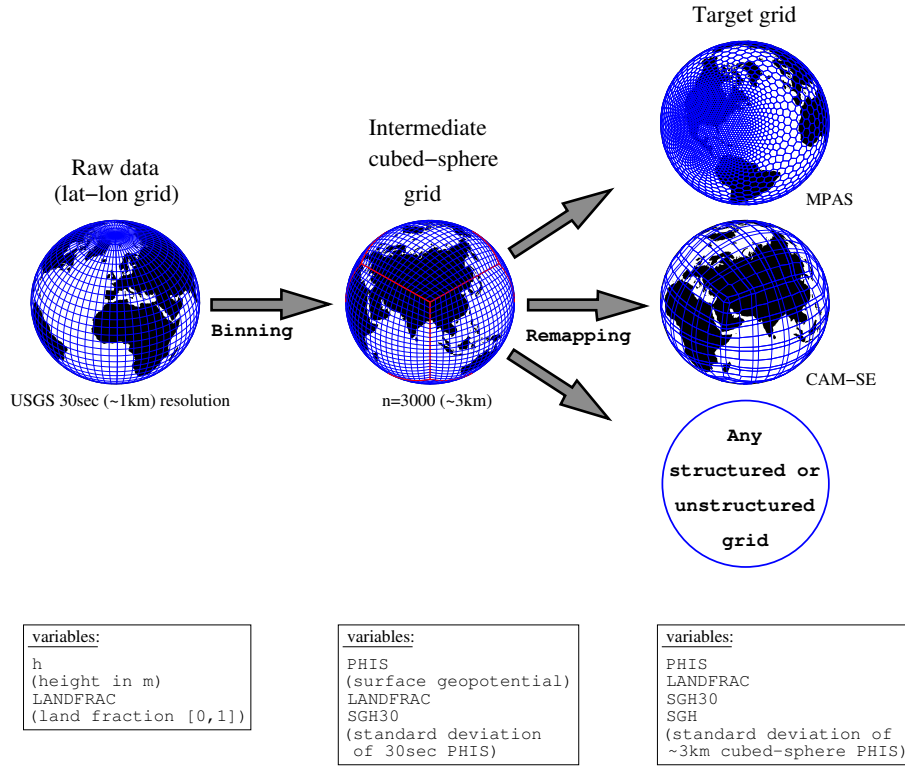


Figure 1. A schematic showing the regridding procedure.

global domain is $6 \times N_c^2$. The grid lines are separated by the same angle $\Delta\alpha = \Delta\beta = \frac{\pi}{2N_c}$ in each coordinate direction.

For notational simplicity the cubed-sphere cells are identified with one index i and the relationship between i and $(icube, jcube, \nu)$ is given by

$$i = icube + (jcube - 1)N_c + (\nu - 1)N_c^2, \quad (7)$$

where $(icube, jcube) \in [1, \dots, N_c]^2$ and $\nu \in [1, 2, \dots, 6]$. In terms of central angles the cubed-sphere grid cell i is defined as

$$A_i = [(icube - 1)\Delta\alpha - \pi/4, icube\Delta\alpha - \pi/4] \times [(jcube - 1)\Delta\beta - \pi/4, jcube\Delta\beta - \pi/4], \quad (8)$$

and ΔA_i denotes the spherical area. A formula for the spherical area ΔA_i of a grid cell on the gnomonical cubed-sphere grid can be found in Appendix C of Lauritzen and Nair (2008) (note that equation C3 is missing arccos on the right-hand side). A quasi-uniform approximately 3km resolution is obtained by using $N_c = 3000$. For more details on the construction of the gnomonic grid see, e.g., Lauritzen et al. (2010).

2.2.1 Step 1: raw elevation data to intermediate cubed-sphere grid ($\Lambda \rightarrow A$)

The ‘raw’ elevation data currently used is the GTOPO30 30 arc second global dataset from the United States Geological Survey (USGS Gesch and Larson, 1998) defined on an approximately 1km regular latitude-longitude grid. The GTOPO30 data comes in 33 tiles (separate files) in 16-bit binary format. Fortran code is provided to convert the data into one NetCDF file. Even though the elevation is stored as integers the size of the NetCDF file is 7GB. The GTOPO file contains height h and landfraction $LANDFRAC$.

The center of the regular latitude-longitude grid cells are denoted $(\lambda_{ilon}, \theta_{jlat})$, $ilon = 1, \dots, nlon$, $jlat = 1, \dots, nlat$. For the USGS dataset used here $nlon = 43200$ and $nlat = 21600$. As for the cubed-sphere we use one index j to reference the grid cells

$$j = ilon + (jlat - 1) \times nlon, \quad j \in [1, \dots, N_r], \quad (9)$$

where $N_r = nlon \times nlat$. The spherical area of grid cell Λ_j is denoted $\Delta\Lambda_j$ and the average elevation in cell j is given by $\bar{h}_{\Lambda_j}^{(raw)}$.

This data is binned to the cubed-sphere intermediate grid by identifying in which gnomonic cubed-sphere grid cell $(\lambda_{ilon}, \theta_{jlat})$ is located. Due to the ‘Cartesian’-like structure

of the cubed-sphere grid the search algorithm is straight forward:

- use the transformation from latitude-longitude coordinates to central angle coordinates described in the Appendix of Nair et al. (2005) to compute the central angles (α, β) corresponding to the mid-point of the latitude-longitude grid cell ($(\lambda_{ilon}, \theta_{jlat})$). [more details on algorithm z]
- the indices of the cubed-sphere cell in which the center of the latitude-longitude grid cell is located is given by

$$\begin{aligned} 305 \quad i_{cube} &= \text{CEILING}\left(\frac{\alpha + \frac{\pi}{4}}{\Delta\alpha}\right), \\ j_{cube} &= \text{CEILING}\left(\frac{\beta + \frac{\pi}{4}}{\Delta\beta}\right), \end{aligned}$$

where the $\text{CEILING}(x)$ function returns the smallest integer not less than x .

The set of indices for which center points of regular latitude-longitude grid cells are located in gnomonic cubed-sphere cell A_i is denoted \mathbb{S}_i . Note that since the USGS dataset is higher resolution than the cubed-sphere \mathbb{S}_i is guaranteed to be non-empty. Through this binning process the approximate average elevation in cubed-sphere cell i becomes

$$315 \quad \bar{h}_{A_i}^{(cube)} = \frac{1}{\Delta A_i} \sum_{j \in \mathbb{S}_i} \bar{h}_{\Gamma_j}^{(raw)} \Delta \Lambda_j. \quad (10)$$

The binning process is straight forward since the cubed-sphere grid is essentially an equidistant Cartesian grid on each panel in terms of the central angle coordinates. This step could be replaced by rigorous remapping in terms of overlap areas between the regular latitude-longitude grid and the cubed-sphere grid using the geometrically exact algorithm of (Ullrich et al., 2009) optimized for the regular latitude-longitude and gnomonic cubed-sphere grid pair or the more general remapping algorithm called SCRIP (Jones, 1999). For convenience the land fraction is also mapped to the intermediate cubed-sphere grid:

$$325 \quad \bar{f}_{A_i}^{(cube)} = \frac{1}{\Delta A_i} \sum_{j \in \mathbb{S}_i} \bar{f}_{\Gamma_j}^{(raw)} \Delta \Lambda_j. \quad (11)$$

The sub-grid-scale variance of elevation with respect to the cubed-sphere grid cell i is

$$330 \quad \text{Var}_{A_i}^{(tms)} = \frac{1}{\Delta A_i} \sum_{j \in \mathbb{S}_i} \left(\bar{h}_{A_i}^{(cube)} - \bar{h}_{\Gamma_j}^{(raw)} \right)^2 \Delta \Lambda_j. \quad (12)$$

- mention the changes to raw data: Caspian sea, Antarctica (why are these changes made?)

TODo: show a Figure illustrating the amount of smoothing performed by the binning!

2.2.2 Step 2: cubed-sphere grid to target grid ($A \rightarrow \Omega$)

The cell averaged values of elevation and sub-grid-scale variances ($\text{Var}_{\Omega}^{(tms)}$ and $\text{Var}_{\Omega}^{(gwd)}$) on the target grid are computed by rigorously remapping the variables from the cubed-sphere grid to the target grid. The remapping is performed using CSLAM (Conservative Semi-LAgrangian Multi-tracer transport scheme) technology (Lauritzen et al., 2010) that has the option for performing higher-order remapping. It is possible to use large parts of the CSLAM technology since the source grid is a gnomonic cubed-sphere grid hence instead of remapping between the gnomonic cubed-sphere grid and a deformed Lagrangian grid, as done in CSLAM transport, the remapping is from the gnomonic cubed-sphere grid to any target grid constructed from great-circle arcs (the target grid ‘plays the role’ of the Lagrangian grid). However, a couple of modifications were made to the CSLAM search algorithm. First of all, the target grid cells can have an arbitrary number of vertices whereas the CSLAM transport search algorithm assumes that the target grid consists of quadrilaterals and the number of overlap areas are determined by the deformation of the transporting velocity field. In the case of the remapping needed in this application the target grid consists of polygons with any number of vertices and the search is not constrained by the physical relation between regular and deformed upstream quadrilaterals. Secondly, the CSLAM search algorithm for transport assumes that the target grid cells are convex which is not necessarily the case for topography target grids. The CSLAM search algorithm has been modified to support non-convex cells that are, for example, encountered in variables resolution CAM-SE; essentially that means that any target grid cell may cross a gnomonic isoline (source grid line) more than twice.

Let the target grid consist of N_t grid cells Ω_k , $k = 1, \dots, N_t$ with associated spherical area $\Delta\Omega_k$. The search algorithm for CSLAM is used to identify overlap areas between the target grid cell Ω_k and the cubed-sphere grid cells A_ℓ , $\ell = 1, \dots, N_c$. Denote the overlap area between Ω_k and A_ℓ

$$\Omega_{k\ell} = \Omega_k \cap A_\ell, \quad (13)$$

and let \mathbb{L}_k denote the set of indices for which $\Omega_k \cap A_\ell$, $\ell = 1, \dots, N_c$, is non-empty. Then the average elevation and variance used for TMS in target grid cell k are given by

$$\bar{h}_{\Omega_k}^{(tgt, raw)} = \frac{1}{\Delta\Omega_k} \sum_{\ell \in \mathbb{L}_k} \bar{h}_{A_\ell}^{(cube)}, \Delta\Omega_{k\ell}, \quad (14)$$

$$\overline{\text{Var}}_{\Omega_k}^{(tms)} = \frac{1}{\Delta\Omega_k} \sum_{\ell \in \mathbb{L}_k} \overline{\text{Var}}_{\Omega_\ell}^{(tms)} \Delta\Omega_{k\ell}, \quad (15)$$

respectively. The variance of the cubed-sphere data $\bar{h}^{(cube)}$ with respect to the target grid cell average values $\bar{h}^{(tgt, raw)}$ is given by

$$\overline{\text{Var}}_{\Omega_k}^{(gwd, raw)} = \frac{1}{\Delta\Omega_k} \sum_{\ell \in \mathbb{L}_k} \left(\bar{h}_{\Omega_k}^{(tgt, raw)} - \bar{h}_{A_\ell}^{(cube)} \right)^2 \Delta\Omega_{k\ell},$$

(16)

The appended superscript *raw* in $\bar{h}^{(tgt,raw)}$ and $\bar{Var}_{\Omega_k}^{(gwd,raw)}$ refers to the fact that the elevation and GWD variance is based on unsmoothed elevation. As mentioned in the introduction the elevation is usually smoothed i.e. the highest wavenumber are removed. This smoothed elevation is denoted

$$\bar{h}^{(tgt,smooth)}. \quad (17)$$

Note that after smoothing the target grid elevation the sub-grid scale variance for GWD should be recomputed as smoothed will add energy to the smallest wavelenghts:

$$\bar{Var}_{\Omega_k}^{(gwd,smooth)} = \frac{1}{\Delta\Omega_k} \sum_{\ell \in \mathbb{L}_k} \left(\bar{h}_{\Omega_k}^{(tgt,smooth)} - \bar{h}_{A_\ell}^{(cube)} \right)^2 \Delta\Omega_{k\ell}. \quad (18)$$

The smoothing of elevation is discussed in some detail in the next section.

2.2.3 Smoothing of elevation $h_{\Omega}^{(tgt)}$

Modeling groups, with the exception of the UK Met Office (Webster et al., 2003a), rarely publish their smoothing procedures and criteria for choosing one level of smoothing over another in peer-reviewed journals. It is likely that qualitative methods are used such as the elimination of visible noise in, e.g. vertical velocity, near topography rather than quantitative diagnostics. The amount of smoothing necessary to remove spurious noise in, e.g. vertical velocity, depends on the amount of inherent or explicit numerical diffusion in the dynamical core (e.g., Lauritzen et al., 2011). It may be considered important that the topographic smoothing is done with discrete operators consistent with the dynamical core so that spurious divergence modes near the grid-scale are not triggered.

In the NCAR-DOE CESM (Community Earth System Model) CAM-FV (Community Atmosphere Model - Finite-Volume; Lin, 2004) the highest wave-numbers are removed by mapping Φ_s (surface geopotential) to a regular latitude-longitude grid that is half the resolution of the desired model resolution, and then mapped back to the model grid by one-dimensional remaps along latitudes and longitudes, respectively, using the PPM (Piecewise Parabolic Method) with monotone filtering.

In CAM-SE (Community Atmosphere Model - Spectral-Elements; Dennis et al., 2012; Neale et al., 2010) the surface geopotential is smoothed by multiple applications of the CAM-SE Laplace operator combined with a bounds preserving limiter. Figure 4 shows different levels of smoothing of surface height for CAM-SE and for comparison CAM-FV. It can clearly be seen that there are large differences between the height of the mountains with different smoothing operators and smoothing strength.

In the global model topography generation software presented here, two approaches for smoothing are offered.

- External smoothing One may provide $\bar{h}^{(tgt,raw)}$ to the dynamical which then smoothes the elevating using internal operators (or a third-party software that smoothes elevation). This method is referred to as external smoothing. If this approach is taken the smoothed elevation $\bar{h}^{(tgt,smooth)}$ must be returned to the topography software for re-computation of the GWD variance since the highest wave-numbers have been removed from the resolved scale and should therefore be included in the sub-grid-scale.

- Internal smoothing algorithm **Julio: please fill in the details; maybe the glory details could be in an Appendix as Section 2 is already quite long ...** A simple smoothing algorithm is provided in the software package referred to as internal smoothing. A filter is applied to the intermediate cubed-sphere elevation data and the smoothed cubed-sphere data is referred to as

$$\bar{h}_{A_i}^{(cube,smooth)}. \quad (19)$$

The reason for applying the smoothing algorithm to the intermediate cubed-sphere data instead of directly on the target grid will become clear (basically it is to make sure that the ridge detection algorithm is consistent). If smoothing takes place on the intermediate cubed-sphere data the smoothed target grid elevation is given by:

$$\bar{h}_{\Omega_k}^{(tgt,smooth)} = \frac{1}{\Delta\Omega_k} \sum_{\ell \in \mathbb{L}_k} \bar{h}_{A_\ell}^{(cube,smooth)} \Delta\Omega_{k\ell}, \quad (20)$$

and the GWD variance is given by (18).

2.2.4 Algorithm for determining the dominant orientation of sub-grid topography

How to deal with variable resolution grids Our algorithm for determining the dominant orientation of sub-grid topography is relatively straightforward. We begin with 3 km topography on the intermediate cubed-sphere grid and compute an extension of each panel on the cubed-sphere via high-order interpolation so that each panel can numerically be treated essentially as a Cartesian computational domain. An outer/model scale (L) is selected. A high-pass filter is optionally applied to remove larger scales. We then take a square of topography $h(x, y)$ with dimension L and rotate it through 16 test angles ξ_i . ‘Padding’ is used to avoid corner effects. In each test rotation a ‘Y’ average is taken to generate a ridge profile $h_i(x)$ at angle ξ_i . The ratio of the variance of h_i to the total 2D variance in $h(x, y)$ is computed. The angle for which this ratio is greatest is designated as the dominant topographic orientation for the sub-grid topography in the $L \times L$ domain of $h(x, y)$. This is done at regular intervals separated by L over

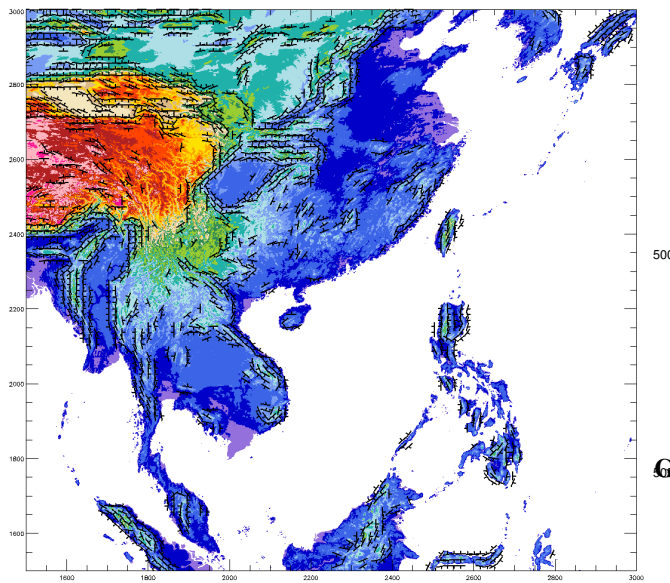


Figure 2. Topography of southeast Asia (color) and diagnosed ridges (black symbols). An outer scale of 50 km is used. Only ridges explaining 50% or more of total 2D variance and possessing maximum vertical displacement of more than 500 m are shown. Long axes of symbols show ridge crests, short appendages indicate direction of greater descent.

510

Acknowledgements. NCAR is sponsored by the National Science Foundation (NSF). Thanks to DOE ...

References

- Bacmeister, J.: Mountain-wave drag in the stratosphere and mesosphere inferred from observed winds and a simple mountain-wave parameterization scheme, *J. Atmos. Sci.*, 50, 377–399, doi:10.1175/1520-0469, 1993.
- Baines, P. and Palmer, T.: Rationale for a new physically based parametrization of subgrid-scale orographic effects, ECMWF Technical Memorandum, 1699, 1990.
- Balmino, G.: The Spectra of the topography of the Earth, Venus and Mars, *Geophys. Res. Lett.*, 20, 1063–1066, doi:10.1029/93GL01214, 1993.
- Beljaars, A., Brown, A., and Wood, N.: A new parametrization of turbulent orographic form drag, *Quart. J. Roy. Meteor. Soc.*, 130, 1327–1347, doi:10.1256/qj.03.73, 2004.
- Bougeault, P., Clar, A. J., Benech, B., Carissimo, B., Pelon, J., and Richard, E.: Momentum Budget over the Pyrénées: The PYREX Experiment, *Bull. Amer. Meteor. Soc.*, 71, 806–818, 1990.
- Bouteloup, Y.: Improvement of the Spectral Representation of the Earth Topography with a Variational Method, *Mon. Wea. Rev.*, 123, 1560–1574, 1995.
- Bouteloup, Y.: Optimal Spectral Topography and Its Effect on Model Climate, *J. Climate*, 9, 2443–2463, 1996.
- Davies, L. and Brown, A.: Assessment of which scales of orography can be credibly resolved in a numerical model, *Quart. J. Roy. Meteor. Soc.*, 127, 1225–1237, doi:10.1002/qj.49712757405, 2001.
- Dennis, Fournier, A., Spotz, W. F., St-Cyr, A., Taylor, M. A., Thomas, S. J., and Tufo, H.: High-Resolution Mesh Convergence Properties and Parallel Efficiency of a Spectral Element Atmospheric Dynamical Core, *Int. J. High Perform. Comput. Appl.*, 19, 225–235, doi:10.1177/1094342005056108, 2005.
- Dennis, J. M., Edwards, J., Evans, K. J., Guba, O., Lauritzen, P. H., Mirin, A. A., St-Cyr, A., Taylor, M. A., and Worley, P. H.: CAM-SE: A scalable spectral element dynamical core for the Community Atmosphere Model, *Int. J. High. Perform. C.*,

510

520

530

540

550

560

570

580

590

595

600

605

610

615

620

625

630

635

640

645

650

655

660

665

670

675

680

685

690

695

700

705

710

715

720

725

730

735

740

745

750

755

760

765

770

775

780

785

790

795

800

805

810

815

820

825

830

835

840

845

850

855

860

865

870

875

880

885

890

895

900

905

910

915

920

925

930

935

940

945

950

955

960

965

970

975

980

985

990

995

1000

1005

1010

1015

1020

1025

1030

1035

1040

1045

1050

1055

1060

1065

1070

1075

1080

1085

1090

1095

1100

1105

1110

1115

1120

1125

1130

1135

1140

1145

1150

1155

1160

1165

1170

1175

1180

1185

1190

1195

1200

1205

1210

1215

1220

1225

1230

1235

1240

1245

1250

1255

1260

1265

1270

1275

1280

1285

1290

1295

1300

1305

1310

1315

1320

1325

1330

1335

1340

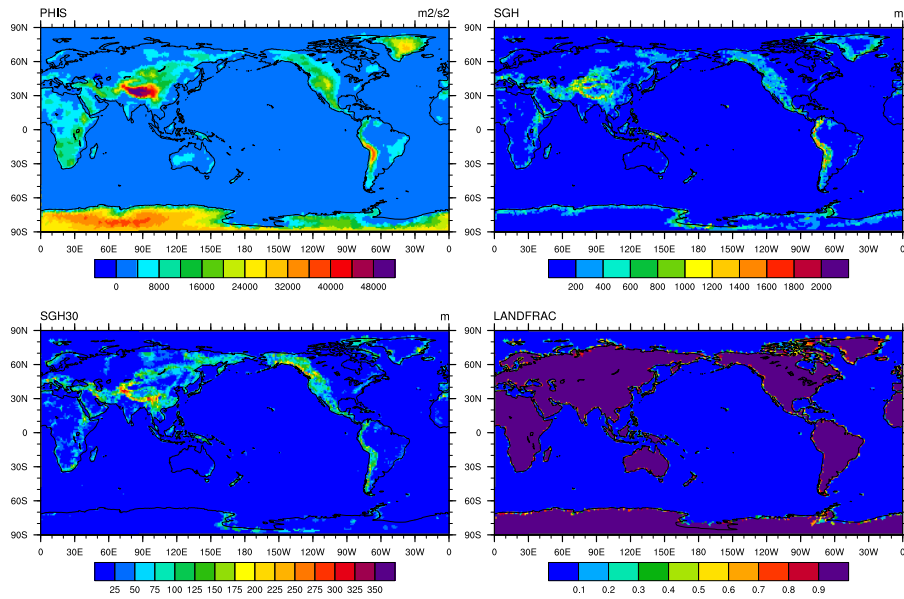


Figure 3. Surface geopotential Φ_s (upper left), SGH (upper right), $SGH30$ (lower left) and $LANDFRAC$ (lower right) for CAM-SE NE30NP4 resolution. The data is plotted on the native grid.

- 26, 74–89, doi:10.1177/1094342011428142, <http://hpc.sagepub.com/content/26/1/74.abstract>, 2012.
- 545 Durran, D.: Numerical Methods for Fluid Dynamics: With Applications to Geophysics, vol. 32 of *Texts in Applied Mathematics*, Springer, 2 edn., 516 p., 2010.
- Eckermann, Y. K. S. and Chun, H.-Y.: An overview of the past, 575 present and future of gravity-wave drag parametrization for numerical climate and weather prediction models: survey article, *Atmosphere-Ocean*, 41, 65–98, doi:10.3137/ao.410105, 2003.
- Farr, T. G., Rosen, P. A., Caro, E., Crippen, R., Duren, R., Hensley, S., Kobrick, M., Paller, M., Rodriguez, E., Roth, L., Seal, D., 580 Shaffer, S., Shimada, J., Umland, J., Werner, M., Oskin, M., Burbank, D., and Alsdorf, D.: The Shuttle Radar Topography Mission, *Reviews of Geophysics*, 45, doi:10.1029/2005RG000183, 2007.
- Fiedler, F. and Panofsky, H. A.: The geostrophic drag coefficient 585 and the ‘effective’ roughness length, *Quart. J. Roy. Meteor. Soc.*, 98, 213–220, doi:10.1002/qj.49709841519, 1972.
- Gesch, D. B. and Larson, K. S.: Techniques for development of 590 global 1-kilometer digital elevation models, in: Pecora Thirteenth Symposium, Am. Soc. Photogrammetry Remote Sens., Sioux Falls, South Dakota, 1998.
- GLOBE Task Team and others: The Global Land One-kilometer 595 Base Elevation (GLOBE) Digital Elevation Model, Version 1.0, <http://www.ngdc.noaa.gov/mgg/topo/globe.html>, 1999.
- Hack, J., Boville, B., Breigleb, B., Kiehl, J., and Williamson, 595 D.: Description of the NCAR Community Climate Model (CCM2), NCAR Technical Note, NCAR/TN-382+STR, doi:10.5065/D6QZ27XV, 1993.
- Janjic, Z.: Pressure gradient force and advection scheme used for forecasting with steep and small scale topography, *Beiträge zur Physik der Atmosphäre*, 50, 186–199, 1977.
- Jones, P. W.: First- and Second-Order Conservative Remapping Schemes for Grids in Spherical Coordinates, *Mon. Wea. Rev.*, 127, 2204–2210, 1999.
- Kim, Y.-J. and Doyle, J. D.: Extension of an orographic-drag parametrization scheme to incorporate orographic anisotropy and flow blocking, *Quart. J. Roy. Meteor. Soc.*, 131, 1893–1921, doi:10.1256/qj.04.160, 2005.
- Lander, J. and Hoskins, B.: Believable scales and parameterizations in a spectral transform model, *Mon. Wea. Rev.*, 125, 292–303., doi:10.1175/1520-0493, 1997.
- Lauritzen, P. H. and Nair, R. D.: Monotone and conservative Cascade Remapping between Spherical grids (CaRS): Regular latitude-longitude and cubed-sphere grids., *Mon. Wea. Rev.*, 136, 1416–1432, 2008.
- Lauritzen, P. H., Nair, R. D., and Ullrich, P. A.: A conservative semi-Lagrangian multi-tracer transport scheme (CSLAM) on the cubed-sphere grid, *J. Comput. Phys.*, 229, 1401–1424, doi:10.1016/j.jcp.2009.10.036, 2010.
- Lauritzen, P. H., Mirin, A., Truesdale, J., Raeder, K., Anderson, J., Bacmeister, J., and Neale, R. B.: Implementation of new diffusion/filtering operators in the CAM-FV dynamical core, *Int. J.*

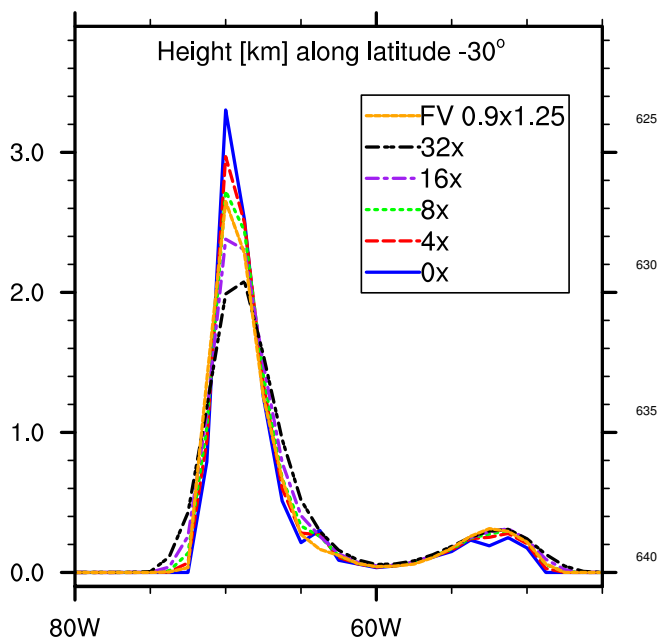


Figure 4. Surface elevation in kilometers for a cross section along 645 latitude 30°S (through Andes mountain range) for different representations of surface elevation. Labels ‘4x’, ‘8x’, ‘16x’ and ‘32x’, refer to different levels of smoothing, more precisely, four, eight, sixteen and thirtytwo applications of a ‘Laplacian’ smoothing operator in CAM-SE, respectively. Label ‘FV 0.9° × 1.25°’ refers to the topography used in CAM-FV. ‘0x’ is the unsmoothed topography on an approximately 1° grid.

High Perform. Comput. Appl., doi:10.1177/1094342011410088, 650 2011.

Lin, S.-J.: A ‘Vertically Lagrangian’ Finite-Volume Dynamical Core for Global Models, Mon. Wea. Rev., 132, 2293–2307, 2004.

600 Lott, F. and Miller, M. J.: A new subgrid-scale orographic drag parametrization: Its formulation and testing, Quart. J. Roy. Meteor. Soc., 123, 101–127, doi:10.1002/qj.49712353704, 1997.

605 McFarlane, N.: The effect of orographically excited gravity wave drag on the general circulation of the lower stratosphere and troposphere, J. Atmos. Sci., 44, 1775–1800, doi:10.1175/1520-0469, 1987.

Mihailović, D. and Janjić, Z.: Comparison of methods for reducing the error of the pressure gradient force in sigma coordinate models, Meteor. Atm. Phys., 35, 177–184, 1986.

610 Nair, R. D., Thomas, S. J., and Loft, R. D.: A Discontinuous Galerkin Transport Scheme on the Cubed Sphere., Mon. Wea. Rev., 133, 814–828, 2005.

Nastrom, G. D. and Gage, K. S.: A Climatology of Atmospheric Wavenumber Spectra of Wind and Temperature Observed by Commercial Aircraft, J. Atmos. Sci., 42, 950–960, 1985.

615 Navarra, A., Stern, W. F., and Miyakoda, K.: Reduction of the Gibbs Oscillation in Spectral Model Simulations, J. Climate, 7, 1169–1183, 1994.

620 Neale, R. B., Chen, C.-C., Gettelman, A., Lauritzen, P. H., Park, S., Williamson, D. L., Conley, A. J., Garcia, R., Kinnison, D.,

Lamarque, J.-F., Marsh, D., Mills, M., Smith, A. K., Tilmes, S., Vitt, F., Cameron-Smith, P., Collins, W. D., Iacono, M. J., Easter, R. C., Ghan, S. J., Liu, X., Rasch, P. J., and Taylor, M. A.: Description of the NCAR Community Atmosphere Model (CAM 5.0), NCAR Technical Note, National Center of Atmospheric Research, 2010.

Richter, J. H., Sassi, F., and Garcia, R. R.: Toward a physically based gravity wave source parameterization in a general circulation model, J. Atmos. Sci., 67, 136–156, doi:dx.doi.org/10.1175/2009JAS3112.1, 2010.

Ronchi, C., Iacono, R., and Paolucci, P. S.: The ‘Cubed Sphere’: A New Method for the Solution of Partial Differential Equations in Spherical Geometry, J. Comput. Phys., 124, 93–114, 1996.

Rutt, I., Thuburn, J., and Staniforth, A.: A variational method for orographic filtering in NWP and climate models, Quart. J. Roy. Meteor. Soc., 132, 1795–1813, doi:10.1256/qj.05.133, 2006.

Scinocca, J. and McFarlane, N.: The parametrization of drag induced by stratified flow over anisotropic orography, Quart. J. Roy. Meteor. Soc., 126, 2353–2393, doi:10.1002/qj.49712656802, 2000.

Thomas, S. J. and Loft, R. D.: The NCAR Spectral Element Climate Dynamical Core: Semi-Implicit Eulerian Formulation, J. Sci. Comput., 25, 307–322, 2005.

Ullrich, P. A., Lauritzen, P. H., and Jablonowski, C.: Geometrically Exact Conservative Remapping (GECoRe): Regular latitude-longitude and cubed-sphere grids., Mon. Wea. Rev., 137, 1721–1741, 2009.

Wallace, J. M., Tibaldi, S., and Simmons, A. J.: Reduction of systematic forecast errors in the ECMWF model through the introduction of an envelope orography, Quart. J. Roy. Meteor. Soc., 109, 683–717, doi:10.1002/qj.49710946202, 1983.

Webster, S., Brown, A., Cameron, D., and Jones, C.: Improvements to the representation of orography in the Met Office Unified Model, Quart. J. Roy. Meteor. Soc., 129, 1989–2010, doi:10.1256/qj.02.133, 2003a.

Webster, S., Brown, A. R., Cameron, D. R., and P.Jones, C.: Improvements to the representation of orography in the Met Office Unified Model, Q. J. R. Meteorol. Soc., 129, 1989–2010, 2003b.

Wood, N., Brown, A., and Hewer, F.: Parametrizing the effects of orography on the boundary layer: An alternative to effective roughness lengths, Quart. J. Roy. Meteor. Soc., 127, 759–777, doi:10.1002/qj.49712757303, 2001.

Zadra, A., Roch, M., Laroche, S., and Charron, M.: The subgrid-scale orographic blocking parametrization of the GEM Model, Atmosphere-Ocean, 41, 155–170, doi:10.3137/ao.410204, 2003.

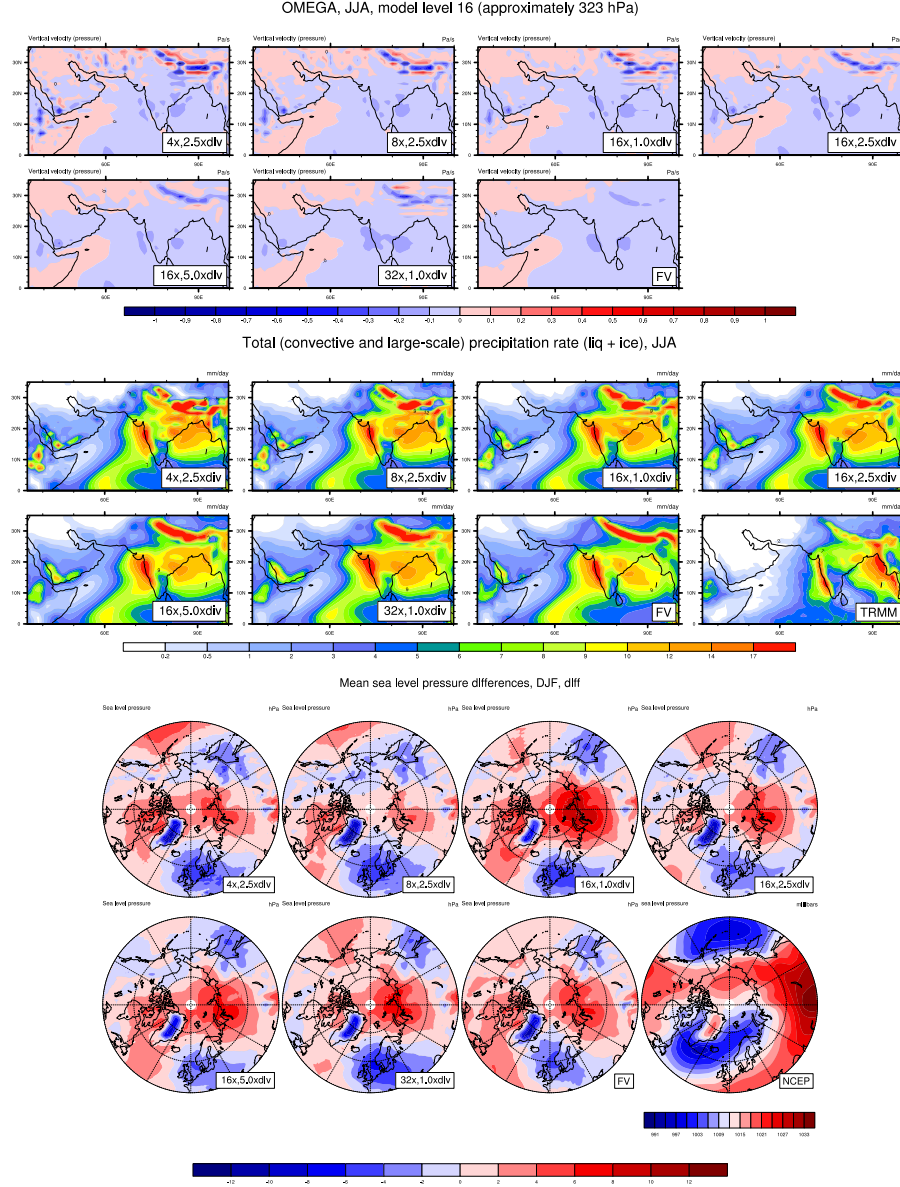


Figure 5. Diagnostics for 30 year AMIP simulations with CAM5.2. Upper, middle and lower group of plots are model level 16 vertical velocity, total precipitation rate and mean sea level pressure differences, respectively. Except for the two right-most plots on the second row of each group of plots, the diagnostics are for CAM-SE with different amounts of smoothing of Φ_s and different levels of divergence damping. The amount of smoothing follows the same notation as Fig. 4 (right) and 1.0 $xdiv$, 2.5 $xdiv$, 5.0 $xdiv$ refers to increasing divergence damping by a factor 1.0, 2.5, and 5.0, respectively. The second right-most plot on each group of plots (labeled FV) show results for CAM-FV. Lower right plot in the second and third group of plots show TRMM observations and NCEP reanalysis data, respectively.

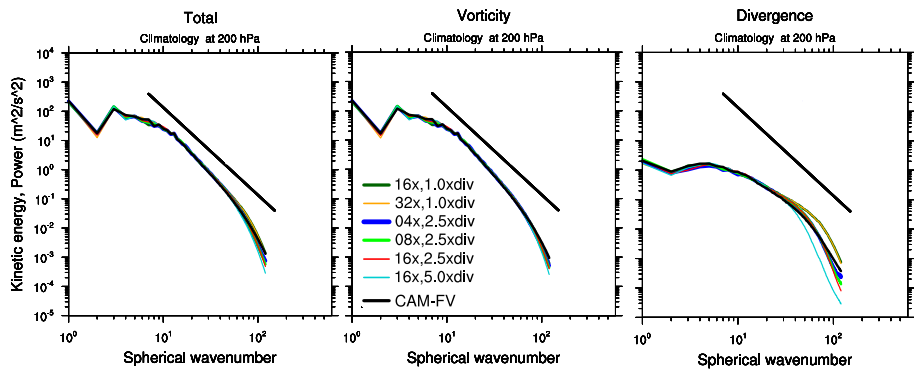


Figure 6. (left) Total kinetic energy spectrum for the velocity field at 200hPa as a function of spherical wavenumber k for CAM-FV and different configurations of CAM-SE. The labeling for the CAM-SE configurations is the same as in Figure 5. The solid-straight black line indicates the k^{-3} reference slope (Nastrom and Gage, 1985). The middle and right plots show the kinetic energy partitioned into divergent and rotational modes, respectively. The spectra have been computed using daily instantaneous wind and surface pressure data for a 2 month period.